

Cite this: *Analyst*, 2017, **142**, 1800

Determination of the transfer function of an atmospheric pressure drift tube ion mobility spectrometer for nanoparticle measurements†

David T. Buckley and Christopher J. Hogan, Jr. *

Drift tube-ion mobility spectrometers (DT-IMSs) are used to separate and characterize the structures of gas phase ions. Recent work in coupling an atmospheric pressure DT-IMS to a condensation particle counter (CPC) has extended the application of drift tube ion mobility spectrometry to nanoparticle analysis, with measurements possible for singly charged particles up to 20 nm in diameter. In examining systems with such large analytes, often of interest is not only separation, but also determination of the nanoparticle size or mobility distribution function, defined as the nanoparticle concentration per unit mobility/size. Distribution function determination requires *a priori* knowledge of the DT-IMS transfer function, *i.e.* the DT-IMS combined transmission and detection efficiency as a function of both mobility and drift/arrival time. The transfer function completely describes analyte transport through an instrument; unfortunately, it has not been experimentally determined in previous work for a DT-IMS. Here, we develop and apply a new method to infer the transfer function of a DT-IMS-CPC system, wherein the system is used to measure particles which are first transmitted through a well-characterized differential mobility analyzer (DMA). The DMA acts as a mobility filter, and only transmits particles within a narrow, well-defined mobility range. From a series of measurements at fixed drift/arrival time (up to 12 seconds) but variable DMA transmission window, DT-IMS-CPC transfer functions are inverted *via* a Twomey–Markowski algorithm. Transfer function inversion reveals that the DT-IMS-CPC system has a resolving power in excess of 10 and upwards of 20. Such resolving powers are in good agreement with model predictions, and are higher than commercially available DMAs in the nanoparticle size range.

Received 23rd February 2017,

Accepted 20th April 2017

DOI: 10.1039/c7an00328e

rsc.li/analyst

1. Introduction

Ion mobility spectrometers (IMSs) temporally or spatially separate charged particles/ions from one another based upon mobility,^{1–4} which is the proportionality constant between an ion's velocity and the external electric field strength.⁵ IMSs are used in a wide variety of gas phase measurements, including but not limited to the detection of explosives,^{6–11} breath analysis,^{12–14} and the characterization of the sizes and structures of inorganic clusters^{15,16} as well as multiprotein complexes.^{17–19} IMSs also find application in determination of the size distribution functions of nanoparticles formed *via* nucleation in ambient air,^{20–22} combustion systems,^{23–26} and plasmas,^{27,28} as well as of nanoparticles aerosolized from colloidal suspensions.^{29,30} In explosive, breath, cluster ion, and protein analysis, it is common to couple IMS with orthogonal

separation techniques, and the objective is typically to identify a specific analyte, or separate structurally distinct analytes.³¹ Therefore, in IMS design, considerable effort is devoted to optimization of an instrument's resolving power,¹ *i.e.* optimization of its ability to identify distinct analytes which have mobilities near one another. In large part, drift tube ion mobility spectrometers (DT-IMSs) have been utilized in such applications; in DT-IMSs ionized analytes traverse a tube with a near-constant axial electric field, and their arrival time at the end of the tube is inversely proportional to their mobility. Theoretically, the resolving power of an idealized DT-IMS instrument is relatively insensitive to the analyte structure, and is moreso dependent upon the DT-IMS dimensions and operating parameters. DT-IMSs have been constructed with resolving powers in excess of 100 (*i.e.* analytes whose mobilities are 1/100th different from one another are distinguishable) and they remain the highest resolving power linear IMS instruments in widespread use today.^{32–36}

However, in using IMSs to determine nanoparticle size distribution functions, high resolving power is more limited in its utility. Nanoparticle size distribution functions are typically

Department of Mechanical Engineering, University of Minnesota, Minneapolis, MN, USA. E-mail: hogan108@umn.edu; Fax: +1-612-625-6069; Tel: +1-612-626-8312

†Electronic supplementary information (ESI) available. See DOI: 10.1039/c7an00328e

continuous and broad (even for “monodisperse” particles),²⁹ hence analyte separation in mobility is less of a concern. Instead, essential for quantitative nanoparticle size distribution function measurements is knowledge of the IMS transfer/transmission function,³⁷ *i.e.* the proportionality constant between measured signal and analyte concentration, as a function of mobility. While the shape of this function is certainly related to the resolving power, it also quantifies the instrument’s mobility-dependent and instrument setting-dependent transmission. The transfer function of IMS devices is not only a function of instrument settings, but also is often mobility-dependent, affected strongly by diffusive motion of analytes during transport through the instrument,³⁸ including at the inlet and outlet. Unfortunately, in utilizing DT-IMSS, instrument transfer functions have been incompletely studied; ideal DT-IMS systems have been described theoretically,^{1,39,40} but limits of detection and dynamic range are typically established through calibration with specific analytes.⁴¹ To our knowledge, procedures have not been developed to determine the transfer/transmission function of a DT-IMS. For this reason, and additionally because conventional DT-IMS arrival times are typically too fast compared to the response times of nanoparticle detectors,⁴² DT-IMSS are not the common IMSS of choice for nanoparticle size distribution measurement. Instead, differential mobility analyzers (DMAs),^{37,43,44} which are spatial mobility filters in which only charged particles in a narrow mobility range traverse from inlet to outlet, are employed in size distribution measurements. Both complete theoretical models and experimental procedures have been developed to determine DMA transfer functions.^{38,45–47} However, there remain issues with the use of DMAs in size distribution measurement, including (1) the need to continuously sweep the instrument operating voltage to transmit particles of variable mobility, which complicates the transfer function,^{47–49} (2) the need for a stable nanoparticle size distribution (*i.e.* rapidly evolving aerosols cannot be examined with a single DMA),⁵⁰ and (3) reduced transmission for higher mobility (higher diffusion coefficient), smaller sized particles.^{38,51}

The aforementioned issues are, in principle, not present in DT-IMS systems, hence their application to nanoparticle size distribution function determination would have advantages over DMAs in many circumstances. Recently, our group has shown that a fluid flow-gated DT-IMS can be interfaced with a single nanoparticle sensitive condensation particle counter (CPC),⁵² extending DT-IMS to singly charged nanoparticle analysis in the 2–20 nm size range.^{53–56} Though proof-of-concept measurements and tandem mobility measurements have been carried out with this instrument, size distribution function analysis still requires knowledge of the DT-IMS-CPC transfer function, and methods need to be developed to determine this function.

Stated more directly, the size distribution function is calculated in IMS from the mobility distribution function, $\frac{dn}{dK}$ (the analyte number concentration per unit mobility, as a function of mobility). In a DT-IMS-CPC measurement, the CPC detects

number of particles per second (N_s) at a specific arrival time, t . The DT-IMS-CPC transfer function, Q_I (which is a function of arrival time t , and mobility K , and incorporates the influences of the detector response time on measurements), links N_s (the measured parameter) and $\frac{dn}{dK}$ (the parameter of interest) *via* a Fredholm integral equation:⁵³

$$N_s = \int_0^{\infty} \frac{dn}{dK} Q_I \eta_c dK \quad (1)$$

where η_c is the mobility dependent activation efficiency of the CPC. Here, we develop and apply new methods to determine Q_I , the DT-IMS-CPC transfer function for singly charged nanoparticles in the sub 20 nm diameter range. We then compare this transfer function to that of conventional differential mobility analyzers in this mobility range.

2. Experimental & numerical methods

2.1. Experimental setup and measurements

The system used to determine the DT-IMS-CPC transfer function is shown in Fig. 1. It consists of a nanoparticle aerosol generation system, a differential mobility analyzer (DMA), the atmospheric pressure, aspirating drift tube ion mobility spectrometer (DT-IMS) in question,⁵³ and two condensation particle counters (CPCs). Polydisperse, charged aerosol particles in the 2–20 nm diameter range were generated *via* charge reduction electrospray (TSI Inc. model 3480 electrospray aerosol generator^{57,58}) of 3 mM sodium iodide dissolved in methanol. The solution was sprayed through a silica capillary (Polymicrotechnologies, Phoenix, AZ, USA) with a 40 μm inner diameter and a 360 μm outer diameter. In charge reduction electrospray, as applied here, the charge distribution of the particles is brought to near steady-state^{59,60} using a Po-210 bipolar ion source (10 mCi), which is incorporated into the electrospray chamber. At this steady-state distribution, the fraction of particles with a net charge is largely a function of particle size (and not chemical composition). Most particles are neutral in the size range examined, and those that are charged have a net charge state of ± 1 unit charge. At these low charge levels and in atmospheric pressure low speed (subsonic) flow, particle charge loss and dissociation before, during, and after measurements are negligible; though these phenomena have been observed for multiply charged nanoparticles⁶¹ and those passing through high pressure drop interfaces.⁶² All generated particles were passed into the DMA. DMA operating principles have been described previously.⁴³ In this study, DMAs were used to isolate particles with inverse mobilities falling within a prescribed range (1×10^5 – 1.5×10^6 V s m²). *Via* the Stokes–Millikan equation,^{63,64} this translates to singly charged particles in the (gas molecule diameter corrected) 4.1–16.8 nm range, and *via* the Mason Schamp equation,⁵ to singly charged particles with collision cross sections in the 21–310 nm² range. These equations are nearly equivalent to one another in

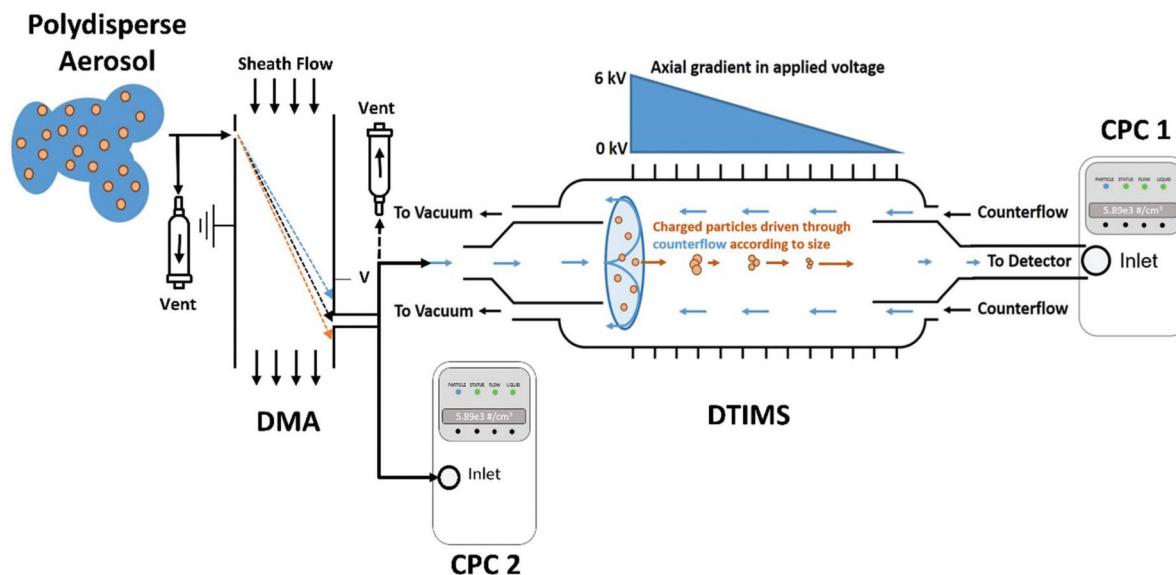


Fig. 1 Schematic of the DMA-DT-IMS-CPC system. DMA: differential mobility analyzer; CPC: condensation particle counter; DT-IMS: drift tube ion mobility spectrometer. The concentration of mono-mobile particles is measured by CPC 2, and an arrival time distribution is measured by the DT-IMS-CPC 1 system. The sample volume of particles/ions is generated by cycling flow into the DT-IMS through the central coaxial tube at the DT-IMS entrance and out of the DT-IMS via the outer coaxial tube, labeled "To Vacuum". Application of an electric potential to the DT-IMS electrodes generates an electric field, which drives the ions within the sample volume across the counterflow.

the size range of interest at atmospheric pressure;⁶⁴ and we report both collision cross sections and mobility diameters simply for completeness. Two DMAs were employed interchangeably in experiments; a TSI Inc. (Shoreview, MN, USA) 3085 nano-DMA⁶⁵ operated with aerosol flowrate of 640 cm³ min⁻¹ and a recirculating sheath flowrate of 11 l min⁻¹ and a half-mini DMA⁴⁴ (Nanoengineering, Boca Raton, FL, USA) operated with an aerosol flowrate of ~5 l min⁻¹ and a sheath flowrate in excess of 100 l min⁻¹. The latter DMA was calibrated using monomobile tetra-alkylammonium⁺ ions, whose mobilities have been well-studied and reported.⁶⁶ However, DT-IMS transfer function results reported are only based upon nano-DMA measurements, as the data analysis approach we applied requires *a priori* knowledge of the DMA transfer function. The half-mini DMA transfer function has not been examined previously in the size range of interest. Half-mini DMA experiments hence served simply served to check the nano-DMA results.

Particles exiting the DMA were first sent into a CPC (TSI model 3786, which applies water as the working fluid and has a $d_{p,50}$, *i.e.*, 50% counting efficiency, for particles with diameters of 2.5 nm)⁶⁷ directly for detection, yielding a number concentration of mobility classified particles, $n_{D|K}$. 60 seconds of signal averaging were employed to obtain $n_{D|K}$, and the standard deviation of the concentration was typically within 3% of the n_D value. Subsequently, flow was diverted and DMA classified particles were sent into the test DT-IMS, coupled with a CPC for detection. The dimensions as well as the flow control scheme of the DT-IMS employed are described in Oberreit *et al.*⁵³ Here, the DT-IMS-CPC was operated with an inlet flowrate

of 640 cm³ min⁻¹, a CPC sampling flowrate of 600 cm³ min⁻¹, a vacuum controlled exhaust flowrate of 920 cm³ min⁻¹, and an inlet counter-flow supply of 880 cm³ min⁻¹. This led to a counter-flowrate of 280 cm³ min⁻¹. Controls were applied to the CPC sampling flowrate, the vacuum exhaust flowrate, and the inlet counter-flowrate supply. This flow control scheme results in an aspirating inlet, wherein particles can be sampled from a stagnant supply. The aspirated, particle-laden flow is constantly cycled into the DT-IMS through the central coaxial tube (seen in Fig. 1) and out of the DT-IMS via the outer coaxial tube (labeled "To Vacuum" in Fig. 1). This forms a sample volume of ions. Upon application of a potential to the DT-IMS electrodes, ions within this sample volume are driven down the DT-IMS toward the detector. A filtered (HEPA) vent at either the entrance or exit of the DMA allowed for maintenance of atmospheric pressure operation of the system while varying the flowrate of aerosol generation.

For DT-IMS-CPC measurements 6 kV was applied across the entire DT-IMS, leading to a near constant axial electric field strength of 2.6×10^4 V m⁻¹. For measurements at each DMA setting (which determines the mobility range for the particles entering the DT-IMS) 10–20 DT-IMS-CPC arrival time distributions were collected in the 1–20 second measurement time range. Such measurements yield arrival time distributions, *i.e.* the particle counts per second, N_s , as a function of measurement time, t . Arrival time distribution measurements were performed for 180 different DMA voltage settings in this study. Reported and analyzed arrival time distributions are the average of all individual arrival time distributions collected for a particular DMA setting.

2.2. Inversion of the drift tube transfer function

Using the aforementioned measurements, Q_I , the DT-IMS-CPC transfer function, was determined as follows. Similar to eqn (1), the CPC-determined number concentration of DMA selected particles, $n_D|_{K^*}$, is related to $\frac{dn}{dK}$, the mobility distribution function of the charge-reduced, electrosprayed particles through a Fredholm integral of the first kind:

$$n_D|_{K^*} = \int_0^\infty \frac{dn}{dK} \theta_D|_{K^*} \eta_C dK \quad (2a)$$

where K^* is the mobility of particles which are maximally transmitted by the DMA (often referred to as the set or classification mobility⁶⁸), and $\theta_D|_{K^*}$ is the DMA transfer function (the fraction of particles transmitted as a function of K for a DMA set to transmit particles about the mobility K^*). K^* is calculable for the (cylindrical) DMA used here from the applied sheath flow (Q_{sh}), applied voltage to the DMA (V), and DMA dimensions (inner and outer radii R_1 and R_2 , respectively, and length L) via the equation: $K^* = Q_{sh} \ln\left(\frac{R_2}{R_1}\right) / (2\pi LV)$. We calculate $\theta_D|_{K^*}$ using the equation provided by Stolzenburg & McMurry,³⁸ which is noted in the ESI.† Because polydisperse particles were generated via charge reduction electrospray, $\frac{dn}{dK}$ is approximately a constant value, $\frac{dn}{dK}|_{K^*}$, over the narrow mobility range where $\theta_D|_{K^*}$ adopts non-negligible values. $\frac{dn}{dK}|_{K^*}$ can hence be calculated as:

$$\frac{dn}{dK}|_{K^*} = \frac{n_D|_{K^*}}{\int_0^\infty \theta_D|_{K^*} \eta_C dK} \quad (2b)$$

Following DMA classification, the DT-IMS-CPC is used to measure the arrival time distribution, $N_S|_{K^*}$ (*i.e.* the particle counts per second). Per eqn (1), $N_S|_{K^*}$ is approximately linked to $\frac{dn}{dK}|_{K^*}$ via the equation:

$$N_S|_{K^*} = \int_0^\infty \frac{dn}{dK}|_{K^*} \theta_D|_{K^*} Q_I \eta_C dK \quad (3)$$

In eqn (3), the product of $\theta_D|_{K^*}$ and $\frac{dn}{dK}|_{K^*}$ is treated as the mobility distribution function of particles entering the DT-IMS; this approximation is commonly invoked in the usage of DMAs as mobility filters.³⁷ All quantities in eqn (3) are known or calculable with the exception Q_I ; thus, Q_I can be inverted from a series of measurements made at various arrival times t and for DMA selected mobilities K^* . Q_I is expected to be a continuous, smooth function of both measurement time and mobility. Unfortunately, Q_I determination is ill-posed; there are more unknowns than knowns (the number of measurements is finite). We therefore opt to employ the Twomey–Markowski algorithm,⁶⁹ as this algorithm has been used extensively in the inversion of size distribution

functions (with equations analogous to eqn (1)) which are both continuous and smooth, from finite measurement sets.

The complete Twomey–Markowski algorithm is outlined in Fig. 2. We first combine eqn (2b) and (3) to yield the parameter $y|_{K^*}$ from measurements:

$$y|_{K^*} = \frac{N_S|_{K^*}}{\frac{dn}{dK}|_{K^*}} = \int_0^\infty \theta_D|_{K^*} Q_I \eta_C dK \quad (4a)$$

However, in making this transformation with measured values, we note that $N_S|_{K^*}$ is sampled digitally, *i.e.* it is determined at specific times, t^* (with a logarithmically scaling sampling rate of order 0.01 ms at minimum in this study). Eqn (4a) is hence discretized as:

$$y|_{t^*, K^*} = \frac{N_S|_{t^*, K^*}}{\frac{dn}{dK}|_{K^*}} = \int_0^\infty \theta_D|_{K^*} Q_I|_{t^*} \eta_C dK \quad (4b)$$

where $y|_{t^*, K^*}$ is calculated from measurements with a specific DMA setting (K^*) at a specific measurement time (t^*), and $Q_I|_{t^*}$ is the transfer function at a specific time and is a function of mobility only. $Q_I|_{t^*}$ is more easily invertible with the Twomey–Markowski algorithm, *i.e.*, by grouping measurements not by

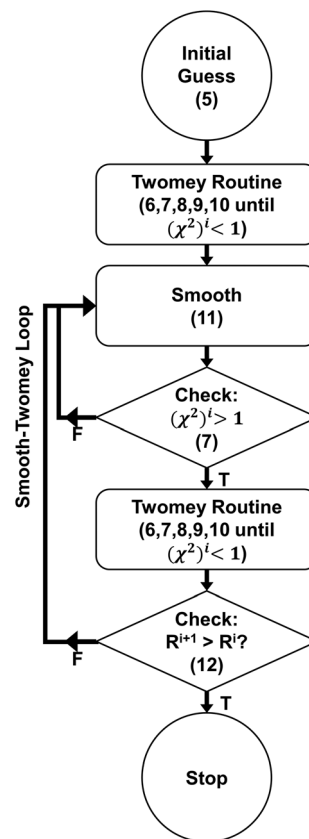


Fig. 2 A schematic depicting the Twomey–Markowski algorithm as applied in this study. Numbers denote the specific equations applied in each step. This flow chart was adapted from Markowski's original work.⁶⁹

K^* but instead by t^* , $Q_1|_{t^*}$ can be approximated using a set of m measurements ($m = 15\text{--}20$) where $y|_{t^*,K^*}$ takes on non-zero values (except at maximum and minimum values of K^*).

$Q_1|_{t^*}$ is analogous to $\theta_D|_{K^*}$; both are functions of mobility for specific instrument settings. In the case of the DMA, the voltage is fixed, while in the case of the DT-IMS, the analogous variable is measurement time. We determined $Q_1|_{t^*}$ for 42 specific t^* values in the range $t^* = 2.5\text{--}12$ seconds. The Twomey–Markowski algorithm consists of several steps: (1) generation of an initial solution, (2) iterative changes to the solution and a test of the solution accuracy, and (3) test of solution roughness. For (1), the initial trial solution ($i = 0$) is generated by assuming the solution is broad in mobility relative to the product of $\theta_D|_{K^*}$ and η_C :

$$Q_1^0|_{t^*} = \frac{y|_{t^*,K^*}}{\int_0^\infty \theta_D|_{K^*} \eta_C dK} \quad (5)$$

Eqn (5) can only be used to generate values at specific DMA set K^* values. Cubic spline interpolation is used to evaluate $Q_1^0|_{t^*}$ at mobilities intermediate to K^* values, leading to $Q_1^0|_{t^*}$ described at $n > m$ specific mobility values. After interpolation, the trial solution is incorporated into the main portion of the algorithm (steps (2) and (3)), *i.e.* the “smooth-Twomey” loop, where it is modified based upon both its accuracy to the original measurement and its roughness. The first step in the smooth-Twomey loop is calculation of a “simulated” measurement value:

$$y_{\text{sim}}^i|_{t^*,K^*} = \int_0^\infty \theta_D|_{K^*} \eta_C Q_1^i|_{t^*} dK \quad (6)$$

where the superscript “ i ” notes the trial number and the subscript “sim” denotes a simulated value. Deviation of the simulated value, $y_{\text{sim}}^i|_{t^*,K^*}$, from the actual measurement, $y|_{t^*,K^*}$, is evaluated through a modified chi-squared test:

$$(\chi^2)^i = \sum_{K^*} \frac{[(y|_{t^*,K^*} - y_{\text{sim}}^i|_{t^*,K^*})/y|_{t^*,\text{max}E}]^2}{m} \quad (7)$$

If $(\chi^2)^i > 1$, the trial solution does not satisfy the error criterion, E (in this study $0.03 < E < 0.06$ was applied). In this case, modifications to the trial solution are computed first by calculating weighting factors which compare the simulated and actual results for each measurement channel:

$$X|_{t^*,K^*} = \frac{y|_{t^*,K^*}}{y_{\text{sim}}^i|_{t^*,K^*}} \quad (8)$$

Next, a correction factor matrix is calculated element-by-element as:

$$C|_{t^*,K^*} = [1 + (X|_{t^*,K^*} - 1)\theta_D|_{K^*}\eta_C] \quad (9)$$

Use of this correction factor matrix ($m \times n$ in dimensions) allows for changes due to trial solution inaccuracy in a specific measurement channel to be distributed maximally at the

mobility pertaining to the measurement channel itself. The $i + 1$ trial solution then is calculated using the correction factors:

$$Q_1^{i+1}|_{t^*} = C|_{t^*,K^*} \times Q_1^i|_{t^*} \quad (10)$$

where multiplication of arrays is performed on an element-by-element basis. Therefore, a trial solution value specific to a mobility K is multiplied several times by factors pertaining both to the accuracy of all measurement channels and their importance in the vicinity of that specific mobility K . After eqn (10) is applied, eqn (6) and (7) are employed again to calculate a new trial instrument response and to test the accuracy of the new trial solution. This cycle of modification (eqn (10)) and testing (eqn (6) and (7)) is repeated until $(\chi^2)^i < 1$; at which point, the trial solution is examined *via* Markowski’s smoothing routine:

$$Q_1^{i+1}|_{t^*}(K_j) = \frac{Q_1^i|_{t^*}(K_{j-1})}{4} + \frac{Q_1^i|_{t^*}(K_j)}{2} + \frac{Q_1^i|_{t^*}(K_{j+1})}{4} \quad (11)$$

where $Q_1^i|_{t^*}(K_j)$ denotes the value of the trial solution for the transfer function at mobility value K_j , and j indexed over all interpolated values (*i.e.* j spans a larger number than m). Because only two values are available for eqn (11) at endpoints, weighting factors of 3/4 and 1/4 were used for the endpoint and its adjacent $j - 1$ or $j + 1$ value, respectively. Markowski’s smoothing routine is applied repeatedly until either $(\chi^2)^i > 1$ (eqn (7)), or a pre-set number of iterations (20, in this analysis) is reached.

The purpose of Markowski’s smoothing routine is to mitigate the roughing effect of eqn (10). The transfer function is expected to be relatively smooth, and discussed by Markowski, for smooth, continuous functions, Twomey’s algorithm often gives rise to solutions which have unphysically high levels of roughness.⁶⁹ After smoothing *via* eqn (11), the trial solution is re-entered into the eqn (6)–(10) cycle. For each trial solution where $(\chi^2)^i < 1$, the roughness (R^i , the average absolute value of the trial solution second derivative) is calculated using the equation:

$$R^i = \left[\sum_{j=2}^{n-1} |Q_1^i|_{t^*}(K_{j+1}) + Q_1^i|_{t^*}(K_{j-1}) - 2Q_1^i|_{t^*}(K_j) \right] / (n - 2) \quad (12)$$

When the roughness is found to increase as compared to the value obtained for the $i - 1$ solution, the smooth-Twomey loop is exited, the $i - 1$ smoothed trial solution is used as the final solution of the Twomey–Markowski algorithm.

3. Results and discussion

3.1. Arrival time distributions

DT-IMS-CPC raw data are in the form of arrival time distributions (*i.e.* N_s , the number of particles counted in a specified time bin divided by bin width in time). The arrival time distributions for DMA selected particles (varying K^*) are plotted in Fig. 3a. Displayed results are the average of at least 10 individual measurements per K^* . Because particles exiting the DMA

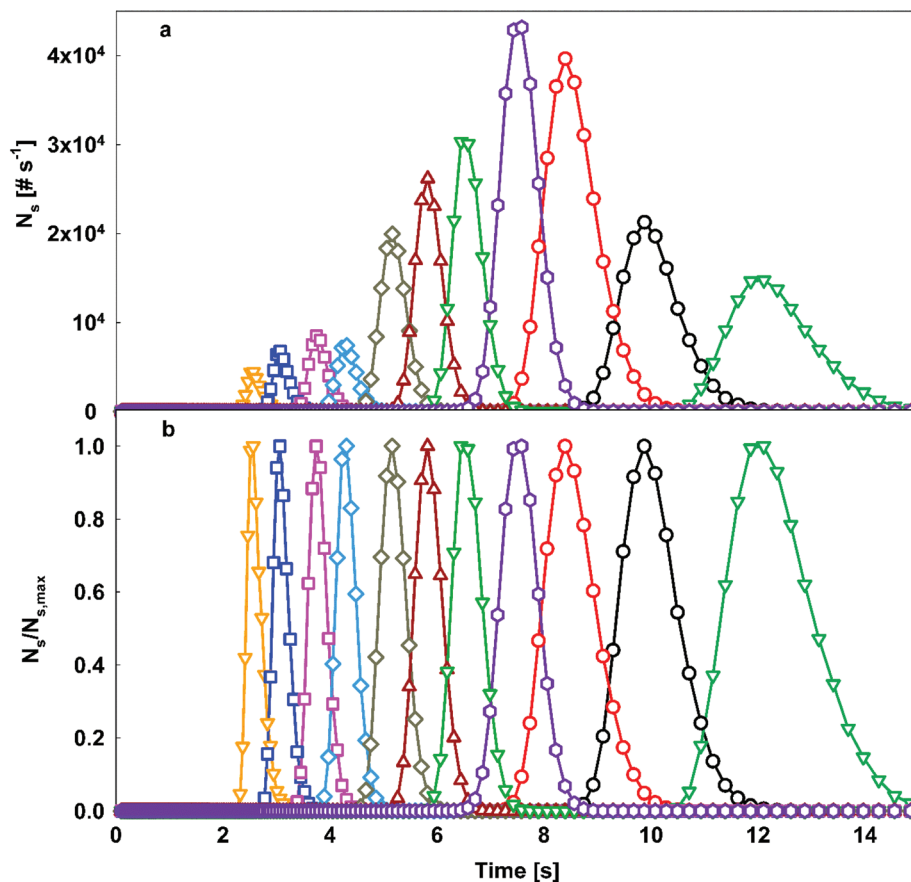


Fig. 3 Selected measured arrival time distributions (a), expressed as N_s with units of number per second, for various DMA settings (K^*). Also shown (b) are the same measured arrival time distributions normalized by their respective maxima.

are relatively monodisperse,³⁷ the arrival time distributions are narrow in time. To better compare the widths of each arrival time distribution to one another, maximum value-normalized arrival time distributions are plotted in Fig. 3b, wherein it is apparent that the arrival time distribution widths increase with decreasing K^* (*i.e.* for larger particles). Though arrival time distributions of DMA selected particles provide a qualitative description of instrument performance, the DT-IMS-CPC transfer function must still be rigorously inferred to quantitatively describe the system. For the inversion process, the distributions of $y|_{t^*,K^*} = \frac{N_s|_{t^*,K^*}}{\left| \frac{dn}{dK} \right|_{K^*}}$ are plotted for selected arrival times

(t^*) in Fig. 4. Distributions are plotted as functions of inverse mobility ($1/K^*$), as inverse mobility is proportional to particle collision cross section⁵ and hence increases with increasing particle size. Prior to performing transfer function inversion, it is important to demonstrate that $y|_{t^*,K^*}$ distributions capture features of the DT-IMS-CPC transfer function. Were the DT-IMS-CPC system of significantly higher resolving power than the DMA, eqn (4a) and (4b) show that normalized $y|_{t^*,K^*}$ distributions would be nearly identical in shape to the DMA

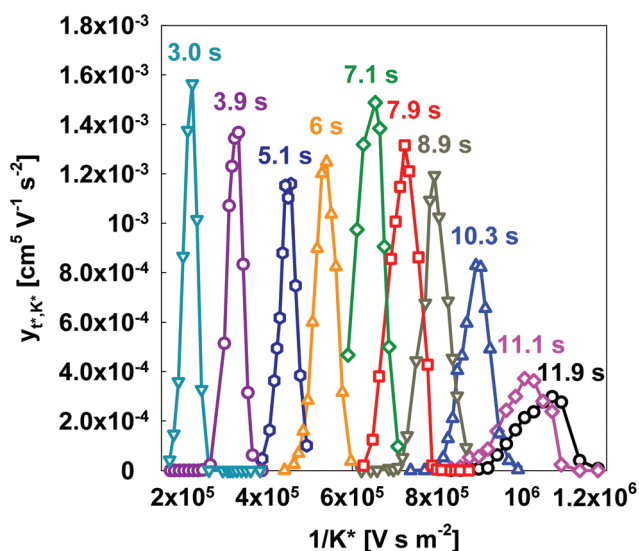


Fig. 4 The parameter $y|_{t^*,K^*}$ plotted as a function of $1/K^*$ for various t^* values (noted above the curves). These values, whose calculation and relevance are described in eqn (4a) and (4b), combine the values measured after the DMA in Fig. 1 and are the inputs to the Twomey–Markowski algorithm.

transfer function, and in this instance the DT-IMS-CPC transfer function could not be inverted from measurements (regardless of the inversion algorithm employed). Discussion of this point is expanded upon in the ESI; in Fig. S1† we plot the nano-DMA transfer function in comparison to $y|_{t^*,K^*}$. This plot shows that $y|_{t^*,K^*}$ distributions are indeed broader than nano-DMA transfer functions and we therefore can employ the Twomey–Markowski inversion routine to infer DT-IMS-CPC transfer functions.

3.2. DT-IMS-CPC transfer functions

As described in the Experimental & numerical methods section, we applied a Twomey–Markowski algorithm to determine the DT-IMS-CPC transfer function, $Q_1|_{t^*}$. We were able to obtain converged $Q_1|_{t^*}$ functions (based on the error criterion employed) for the 42 t^* values examined. To our knowledge this is the first effort wherein a Fredholm integral equation inversion technique has been employed to evaluate the transfer function of a mobility-based measurement system and is the first attempt to determine the transfer function for a DT-IMS. For comparison, in experimentally determining DMA transfer functions, Stratmann *et al.*⁴⁵ and Birmili *et al.*⁷⁰ utilized a non-linear least squares approach to determine coefficients built into a predefined functional form. Li *et al.*⁷¹ extended this approach to define the DMA transfer function in a linear piece-wise manner. Here, the DT-IMS-CPC transfer function has no assumed functional form *a priori*. Jiang *et al.*⁴⁶ used strictly monomobile particles to determine DMA transfer functions; this approach as well cannot be applied here due to lack of monomobile standards in the mobility range of interest.

Fig. 5 displays selected inverted transfer functions. They are plotted as functions of inverse mobility for different measurement times, and they quantify the transmission characteristics of the DT-IMS-CPC system at these different times. The trans-

fer functions are smooth and all appear to be skewed towards higher mobilities/smaller inverse mobilities. This skew can be explained by the higher diffusion coefficients of smaller particles. Smaller particles diffusively deviate from their mobility-dependent trajectories and are thus more likely to be detected at wider range of t^* values. This skewness is also present in the transfer functions of other mobility classification devices, including DMAs,³⁸ but for DMAs it is much less pronounced than is observed here. This increased skewness in transfer functions, as a result of diffusion in the DT-IMS-CPC, is most likely due to the increased residence time in the instrument (1–10 s for DT-IMS-CPC compared to ~ 0.05 s in a DMA).

The inverted transfer functions also vary in both peak value and width. Increases in transfer function absolute width with t^* are expected for DT-IMS systems, which typically have drift time independent resolving powers. However, additional relative transfer function broadening at smaller t^* is brought about by the response time distribution function of the CPC in the examined system. Uniquely narrow transfer functions were obtained in the $t^* = 8$ –9 second range (with $t^* = 8.4$ seconds shown in Fig. 5); further investigation (primarily using numerical models of the flow and electric fields in the DT-IMS) will be needed to understand what leads to such narrow transfer functions in this time range. Generally, we find that as the transfer function width narrows, the peak value increases, leading to overall similar transmission (total transfer function area).

The peak in inverse mobility of each transfer function is plotted as a function of t^* in Fig. 6a along with a linear fit (black line). The observed linearity agrees with theory as well as with previous measurements.^{1,53} Fig. 6b displays DT-IMS-CPC (green circles) and TSI nano-DMA resolution as a function of both inverse mobility and measurement time.^{38,65} For the nano-DMA, only the inverse mobility axis is applicable, while for the DT-IMS-CPC, measurement time and inverse mobility are linked *via* the relationship noted in Fig. 6a. In

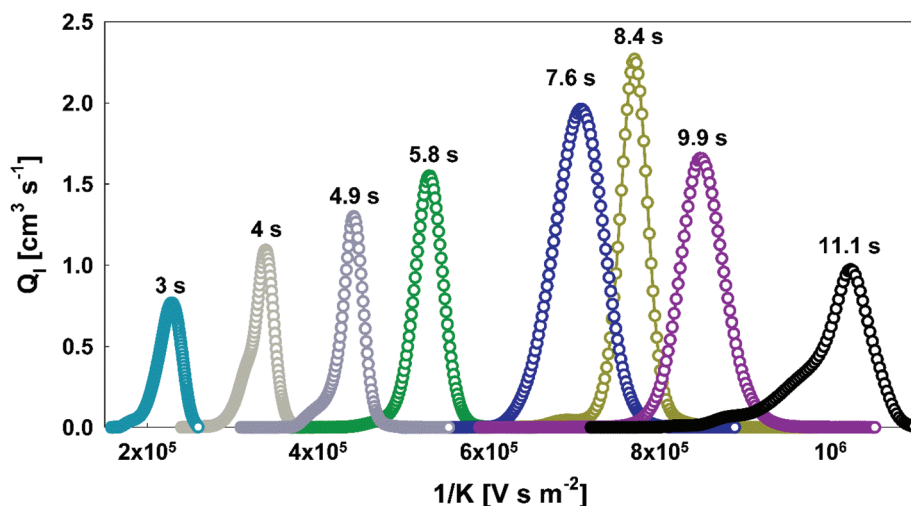


Fig. 5 Selected inverted DT-IMS-CPC transfer functions, $Q_1|_{t^*}$. t^* is noted for each displayed transfer function.

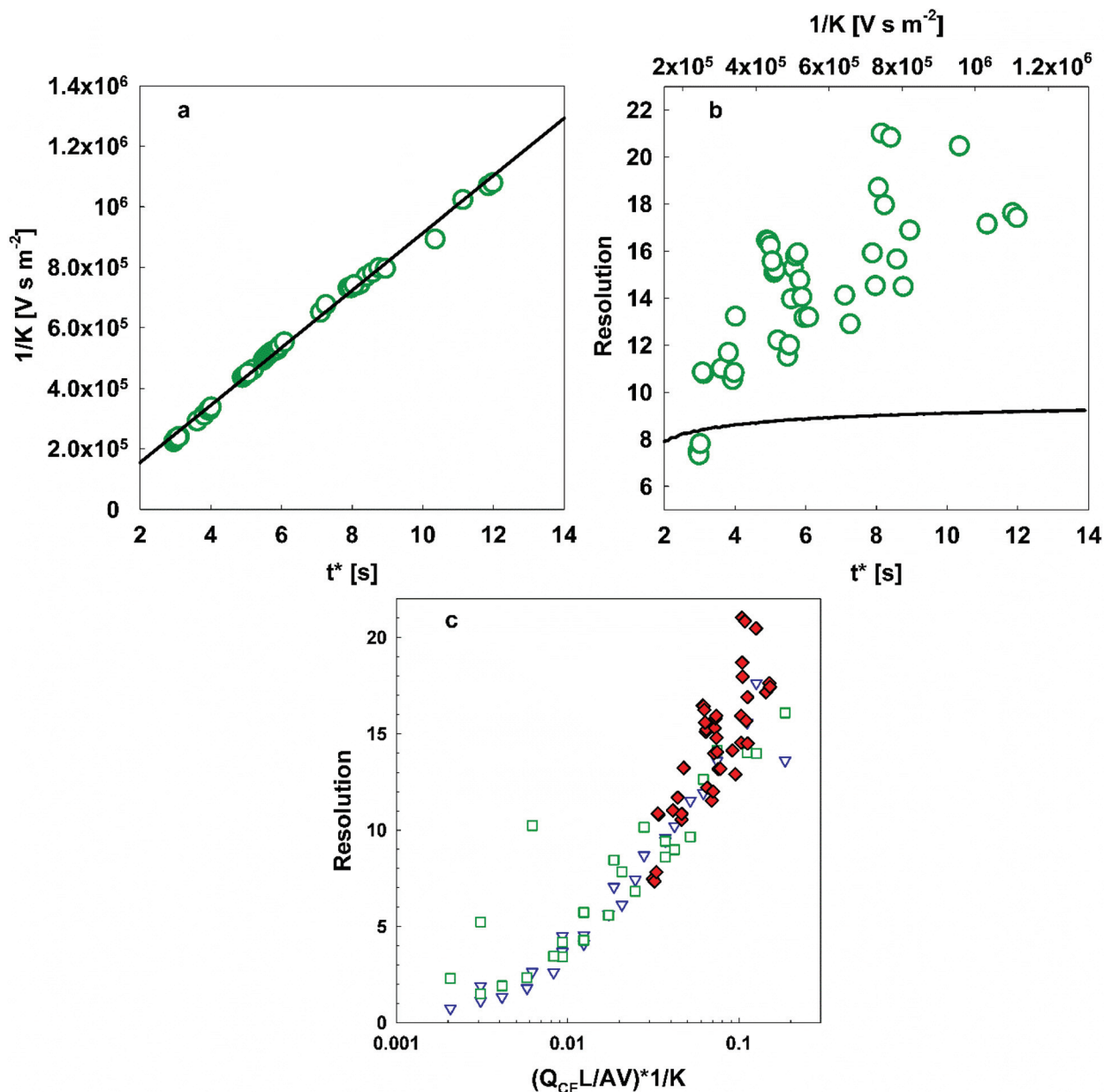


Fig. 6 (a.) The inverse mobility corresponding to the centroid of the DT-IMS-CPC transfer as a function of t^* . (b.) Resolution, defined as the ratio of the centroid inverse mobility to the FWHM of the transfer function, as a function of t^* for the DT-IMS-CPC (green circles) and for the TSI nano-DMA (black line) as a function of inverse mobility (upper horizontal axis). The nano-DMA resolution was calculated assuming that the particles were singly charged, and the upper and lower horizontal axes are aligned in accordance with the relationship defined in (a.). (c.) A comparison of the experimentally inferred resolution (red diamonds) to predictions from Oberreit *et al.* (2014),⁵³ green squares—results of numerical simulations; blue triangles—analytical modeling. $(Q_{CF} L/AV) \times 1/K$ is a dimensionless parameter defined in the main text.

both instances, resolution is defined as the ratio of the peak inverse mobility in the transfer function to the transfer function's full width at half maximum. The nano-DMA resolution was calculated assuming singly charged particles, an aerosol-to-sheath flowrate ratio of 0.1, and again using the equations of Stolzenburg and McMurry.³⁸ Apparent in the figure, DT-IMS-CPC resolution increases with measurement time/inverse mobility over the studied range. As commented on in

the preceding paragraph, the lower resolutions at smaller measurement times are attributable to the influence of the CPC response time distribution function (which is distributed about a mode value of 0.85 s)⁵³ and may also be attributable to diffusional broadening of the analyte sample packet for higher mobility (smaller size) particles. For the nano-DMA, the resolution decreases slightly at lower inverse mobility; this is due to more pronounced diffusional broadening of small particles as

they traverse the DMA. Though a secondary issue in determining instrument transfer functions and using for size distribution function inversion, overall, the results displayed in Fig. 6b demonstrate that the DT-IMS-CPC system is in general, a higher resolving power instrument than are conventional DMAs (*i.e.* DMAs which operate with aerosol-to-sheath flowrate ratios of 0.1 or more).

In Fig. 6c, we plot the transfer function resolution as a function of the dimensionless ratio $(Q_{CF}L/AV) \times 1/K$, where Q_{CF} is the counter-flowrate ($280 \text{ cm}^3 \text{ min}^{-1}$), L is the drift tube length (22.8 cm), A is the DT-IMS cross sectional-area (12.57 cm^2), V is the applied voltage (6 kV) and $1/K$ is the inverse mobility. Also plotted are the predicted resolutions from Oberreit *et al.*⁵³ based upon both trajectory simulations of particles and a simplified analytical model of the DT-IMS-CPC system. Both the simulations and model calculations apply to the conditions used in this study. We find strong agreement between the previously calculated and transfer function inferred resolutions. Interestingly, Oberreit *et al.*⁵³ experimentally estimated lower resolutions of the DT-IMS-CPC system. However, these estimates neglected the influence of the DMA transfer function on DMA-DT-IMS-CPC measurements, *i.e.* their resolution estimations were based upon the widths of arrival time distributions (which are broadened by both the DMA and DT-IMS). The agreement observed here between measured and calculated resolution suggests both that the DT-IMS-CPC system performs as expected based upon its design and also gives credence to the application of the Twomey–Markowski method for transfer function inference.

3.3. Transfer function parameterization

Use of eqn (1) for size distribution function inversion requires knowledge of the DT-IMS-CPC transfer function continuously in both t^* and K . However, the analysis presented thus far has only provided a finite, discrete description of the transfer function in t^* . We hence opted to fit and parameterize the experimentally-determined transfer functions with skewed Gaussian curves, enabling their continuous description in t^* and K . A skewed Gaussian distribution can be described simply as a Gaussian distribution multiplied by its cumulative distribution function. The equation for a skewed Gaussian distribution is provided in the ESI;† it is defined by its location (m), scale (s), amplitude (A), and skew (α). The transfer functions for mobility based measurement instruments have not been described by skewed Gaussian distributions previously (others have used lognormal distributions³⁸); however, we find this function most appropriate to capture features of such transfer functions. To determine the best-fit parameters for each experimentally-determined transfer function (Q_i), we first determined the relationship between skew and t^* . All experimentally-determined transfer functions were normalized in magnitude as well as location (*i.e.*, they were centered around 1.0 with peak around 1.0). The resulting data were fitted parametrically by applying MATLAB's non-linear fitting procedure to eqn (S5) of ESI,† giving values of m , s , A , and α for normal-

ized transfer functions. The skew parameter inferred in this manner is not influenced by the normalization, though the other parameters are. As shown in Fig. S2 of the ESI,† α and t^* are not well correlated (except at large measurement times); henceforth the mean value of α of -2.14 (with negative values indicative of a skew towards smaller inverse mobilities) was applied to all fit functions.

Following determination of α , the original (non-normalized) transfer function data were fitted to eqn (S5)† with α held constant. This procedure resulted in data relating the remaining three parameters (m , s , and A) to t^* . These results are provided in Table 1, and are plotted in the ESI (Fig. S2a–f†). Use of these curves enables the continuous description of the DT-IMS-CPC transfer function for mobility and size-distribution function inversion. Fig. 7 compares selected, inverted Q_i to their functional forms calculated with skewed Gaussian fits, showing that skewed Gaussians capture well the features of DT-IMS-CPC transfer functions.

3.4. Theoretical comparison and the effects of non-idealities

Though the resolving powers inferred from measurements agree well with theoretical estimates,⁵³ non-idealities in flow and electric fields can have an influence on system behavior, which are difficult to incorporate into theoretical descriptions.^{39,40} Here we attempt to better understand how non-idealities influence system performance and also to decouple the effects of the CPC from the DT-IMS on the overall transfer function. To do so, first, we present a derivation for eqn (1), representing the relationship between the measured arrival time distribution, N_s , and the original mobility distribution function, $\frac{dn}{dK}$. Previous derivations of this relationship have been performed, but they resulted in a Fredholm integral equation with time as the integrating variable,⁵³ and hence do not apply to eqn (1). We define $\frac{dn}{dK}$, V_s , and η_T respectively as the number-concentration-based mobility distribution function of the original aerosol (prior to DT-IMS entrance), the sample volume, and the transmission efficiency of particles

Table 1 A summary of the Gaussian parameter values which define the fitted DT-IMS-CPC transfer function. Parameter values are shown for a range of t^* values, including the location, m , scale, s , amplitude, A , and the parameter most related to skew, α . The equation of a skewed Gaussian function is provided in the ESI

| t^* [s] | m [V s m^{-2}] | s [V s m^{-2}] | A [$\text{cm}^3 \text{ s}^{-1}$] | α (const) |
|-----------|-----------------------------|-----------------------------|--------------------------------------|------------------|
| 3 | 2.53×10^5 | 1.72×10^4 | 1.29 | -2.14 |
| 4 | 3.52×10^5 | 2.02×10^4 | 1.74 | -2.14 |
| 5 | 4.51×10^5 | 2.33×10^4 | 2.18 | -2.14 |
| 6 | 5.49×10^5 | 2.65×10^4 | 2.63 | -2.14 |
| 7 | 6.48×10^5 | 2.98×10^4 | 3.08 | -2.14 |
| 8 | 7.47×10^5 | 3.01×10^4 | 3.53 | -2.14 |
| 9 | 8.46×10^5 | 3.32×10^4 | 3.97 | -2.14 |
| 10 | 9.44×10^5 | 3.74×10^4 | 3.10 | -2.14 |
| 11 | 1.04×10^6 | 4.34×10^4 | 1.95 | -2.14 |
| 12 | 1.14×10^6 | 6.01×10^4 | 1.29 | -2.14 |
| 13 | 1.24×10^6 | 9.11×10^4 | 0.918 | -2.14 |

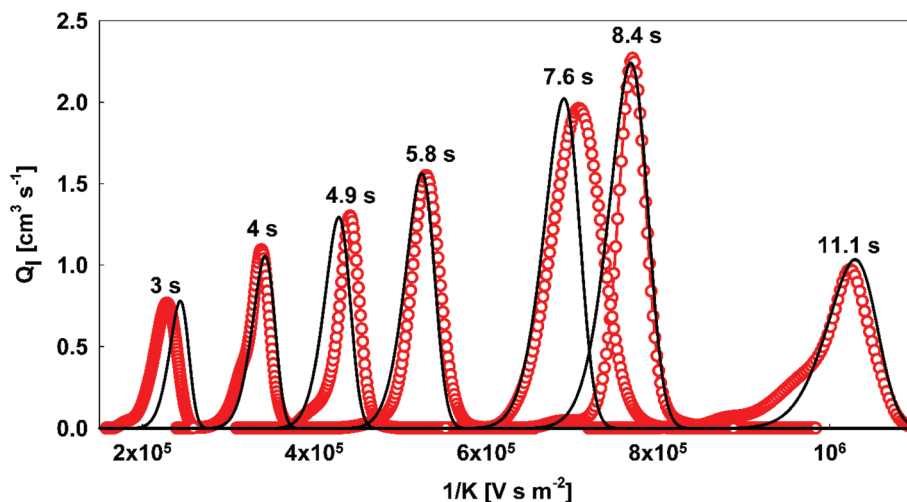


Fig. 7 Selected inverted DT-IMS-CPC transfer functions (red circles), in comparison to skewed Gaussian fits (black lines).

through the inlet of the DT-IMS and into the sample volume, respectively. The sample volume represents the volume occupied by particles which are able to transit across the drift region upon application of the electric potential. The total number of particles inside the sample volume of mobility K to $K + dK$ is thus $\eta_T V_s \frac{dn}{dK} dK$. The transmission of particles with mobility K across the drift region to the detector is distributed in drift time t_d (the time required to transit the drift tube, but not including the transit time with the CPC) by θ_1 . θ_1 was derived previously⁵³ (and is noted in the ESI†) through modification of the original derivation by Revercomb and Mason¹ by accounting for the counter flow velocity of the drift gas as well as the non-zero width of the sample volume. The number of particles from the sample volume with mobility K to $K + dK$ which traverse the drift tube in time t_d to $t_d + dt_d$ is then:

$$dN(t_d, K) = \eta_T V_s \frac{dn}{dK} \theta_1 dK dt_d \quad (13)$$

Upon traversing the drift tube, particles enter the CPC, which has a time-distributed response function (also previously described⁵³ and provided in the ESI†), defined as Φ_C . Φ_C depends upon t_C , defined as $t_C = t^* - t_d$ with $dt_C = dt^*$. Then, the number of particles with previously described range of mobility which are detected per unit time, dN/dt^* , is:

$$\frac{dN(t^*, t_d, K)}{dt^*} = V_s \frac{dn}{dK} \eta_T \eta_C \eta_A \theta_1 \Phi_C dK dt_d \quad (14)$$

where η_C is the counting efficiency of the CPC and η_A is the transmission efficiency of the DT-IMS-CPC system. Accounting for the contribution of particles of all drift times less than that of the measurement time yields:

$$\frac{dN(t^*, K)}{dt^*} = \left[V_s \frac{dn}{dK} \eta_T \eta_C \eta_A \int_0^{t^*} \theta_1 \Phi_C dt_d \right] dK \quad (15)$$

The total number of particles detected per unit time at measurement time t^* is determined by integrating over all mobilities:

$$N_s = \frac{dN(t^*)}{dt^*} = \int_0^\infty \left[V_s \frac{dn}{dK} \eta_T \eta_C \eta_A \int_0^{t^*} \theta_1 \Phi_C dt_d \right] dK \quad (16)$$

Eqn (16) is of the same form as eqn (1), and through comparison to eqn (1), the definition of $Q_I|_{t^*}$ is clear:

$$Q_I|_{t^*} \cong V_s \eta_T \eta_C \eta_A \int_0^{t^*} \theta_1 \Phi_C dt_d \quad (17)$$

All of the terms on the right hand side of eqn (17) can be described theoretically or have been estimated previously.^{53,72} However, calculations based upon them will fail to agree with parameterized transfer functions, particularly in width and amplitude. This disagreement is somewhat expected, because the functions input into eqn (17) are based on idealized models of the DT-IMS-CPC system, and hence neglect multi-dimensional effects (*i.e.* models to-date have assumed the geometry is perfectly axisymmetric), the specific shape of the sample volume, mobility dependencies to the sample volume, and wall influences on both the flow and electric field profiles in the drift tube. A functional representation of these additional effects would permit CPC interchangeability; for any CPC response time distribution Q_I could be calculated if all other terms in eqn (17) were well-described. We hence modify eqn (17) to introduce a correction function $f_c(t^*, K)$:

$$Q_I|_{t^*} = \int_0^{t^*} f_c \theta_1 \Phi_C dt_d \quad (18)$$

This formulation defines the transfer function in such a way that all variables except $f_c(t, K)$ are known *a priori*. It is then possible to determine a representation of $f_c|_{1/K}$ through the same inversion methods described previously in this work; to

do so for a specific inverse mobility, we express $Q_{I|1/K}$ as a function of t^* (the converse of $Q_{I|t^*}$) using the parameterized skewed Gaussian distributions. The Twomey–Markowski algorithm was employed again using $Q_{I|1/K}$ as the input ‘measurement’, and we calculated the product $\theta_t \Phi_C$ using the functions provided in the ESI.† The conditions described the inversion of the drift tube transfer function section were used for convergence of the algorithm as in original $Q_{I|t^*}$ determination.

Selected correction functions are plotted in Fig. 8 for various inverse mobilities, $1/K$. They are slightly asymmetric and vary in magnitude for varying mobilities, again indicating there are compounding time and mobility-dependent factors influence transmission through the DT-IMS-CPC system. Nonetheless, should a different response time CPC be used with the tested DT-IMS, $Q_{I|t^*}$ functions can be calculated using $f_c|_{1/K}$, θ_t , and the new Φ_C distribution function in eqn (18).

3.5. Comparison to differential mobility analysis

A final comparison is between the DTIMS and commercial DMA transfer functions in the tested inverse mobility range. Fig. 9 displays coincidental DT-IMS-CPC and calculated nano-DMA transfer functions (*i.e.* those with resolutions plotted in Fig. 6b) in terms of both inverse mobility and singly charged mobility equivalent diameter (*via* the Stokes–Millikan equation). For this plot, the DT-IMS-CPC transfer functions (which are dimensional) have been normalized to have the same integral area as the DMA transfer functions. The higher resolution of the DT-IMS-CPC transfer functions in comparison to nano-DMA is apparent in Fig. 9, as is the skewness of the DT-IMS-CPC transfer functions.

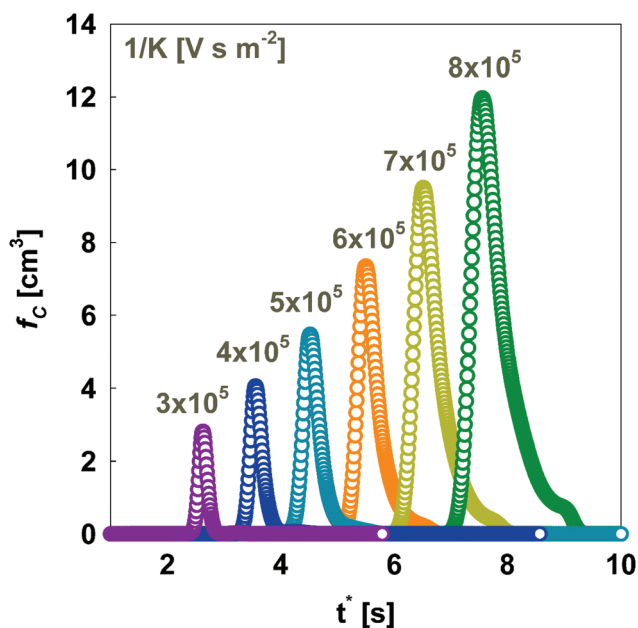


Fig. 8 The transfer function correction factor plotted as a function of t^* for various mobility values.

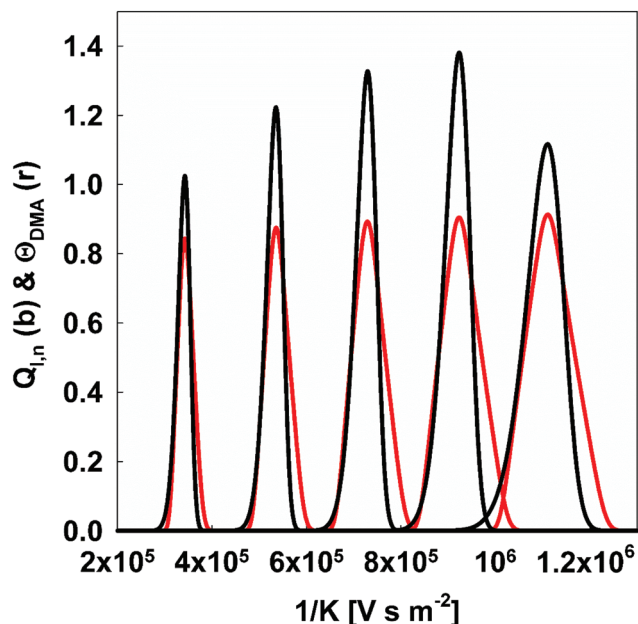


Fig. 9 Normalized DT-IMS-CPC transfer functions (black) and nano-DMA transfer functions (red). DT-IMS-CPC transfer functions were normalized to have the same integral area as the DMA transfer functions and same peak in inverse mobility.

4. Conclusions

The transfer function for an atmospheric pressure, fluid-mechanically gated drift tube ion mobility spectrometer (DT-IMS) coupled to a condensation particle counter (CPC) has been determined for the first time from experimental measurements combined with the Twomey–Markowski inversion algorithm. Based on the inferred transfer functions, we make the following concluding remarks:

1. The Twomey–Markowski algorithm can be applied to infer the transfer functions of mobility measurement systems instances where a mobility filter (such as a DMA, overtone mobility spectrometer,⁷³ or transverse modulation ion mobility spectrometer⁷⁴) is used to pre-select analytes to be measured by the IMS instrument under examination. Transfer function determination is critical for instruments applied to measure continuous mobility distribution functions, as in the case for nanoparticles or extremely heterogeneous ion populations, wherein an IMS is used without other separations schemes and all ion peaks are not discernable from one another.⁷⁵ The method applied here may also find potential application in better describing the transfer functions of scanning DMAs⁴⁷ and multichannel detector instruments.^{76,77}

2. A DT-IMS-CPC combination can be formed which has a narrower transfer function (higher resolving power) than a conventional DMA and can be applied to nanoparticles. Improvements to both the DT-IMS (*i.e.* higher operating voltage) and CPC (narrower response time distribution) would lead to an even higher resolution instrument; future DT-IMS-CPC systems may have resolving powers approaching

those commonly applied to small ions with electrical detectors. The transfer function is sensitive to DT-IMS-CPC operating conditions, and the transfer function would need to be redetermined (using the same approach) if the DT-IMS was operated with different flowrates or applied voltage than those used in this study.

3. DT-IMS-CPC transfer functions display a skew towards smaller inverse mobilities and have mobility dependent peak values. While improved modeling efforts may aid in understanding why such mobility dependencies arise, we argue that the measurement and data inversion approach applied here is essential in fully describing an instrument's performance *via* its transfer function.

Acknowledgements

This work was supported by Kanomax USA as well as the United States Army Research Office Award MURI W911NF-12-0407. The authors thank Dr Derek Oberreit (Kanomax FMT) and Dr Nobuhiko Fukushima (Kanomax Japan) for their advice and suggestions on DT-IMS-CPC measurements.

References

- 1 H. E. Revercomb and E. A. Mason, *Anal. Chem.*, 1975, **47**, 970–983.
- 2 H. H. Hill, W. F. Siems and R. H. St. Louis, *Anal. Chem.*, 1990, **62**, 1201A–1209A.
- 3 P. Dugourd, R. R. Hudgins, D. E. Clemmer and M. F. Jarrold, *Rev. Sci. Instrum.*, 1997, **68**, 1122–1129.
- 4 H. Borsdorf, T. Mayer, M. Zarejousheghani and G. A. Eiceman, *Appl. Spectrosc. Rev.*, 2011, **46**, 472–521.
- 5 E. A. Mason and E. W. McDaniel, *Transport Properties of Ions in Gases*, Wiley, New York, 1988.
- 6 M. Mäkinen, M. Nousiainen and M. Sillanpää, *Mass Spectrom. Rev.*, 2011, **30**, 940–973.
- 7 M. Tam and H. H. Hill, *Anal. Chem.*, 2004, **76**, 2741–2747.
- 8 G. R. Asbury, J. Klasmeier and H. H. Hill Jr., *Talanta*, 2000, **50**, 1291–1298.
- 9 R. G. Ewing, D. A. Atkinson, G. Eiceman and G. Ewing, *Talanta*, 2001, **54**, 515–529.
- 10 D. S. Moore, *Rev. Sci. Instrum.*, 2004, **75**, 2499–2512.
- 11 W. E. Steiner, S. J. Klopsch, W. A. English, B. H. Clowers and H. H. Hill, *Anal. Chem.*, 2005, **77**, 4792.
- 12 J. I. Baumbach, *J. Breath Res.*, 2009, **3**.
- 13 W. Vautz, J. Nolte, R. Fobbe and J. I. Baumbach, *J. Breath Res.*, 2009, **3**.
- 14 M. Westhoff, P. Litterst, L. Freitag, W. Urfer, S. Bader and J. I. Baumbach, *Thorax*, 2009, **64**, 744–748.
- 15 J. W. J. Wu, R. Moriyama, H. Tahara, K. Ohshimo and F. Misaizu, *J. Phys. Chem. A*, 2016, **120**, 3788–3796.
- 16 K. Ohshimo, T. Komukai, R. Moriyama and F. Misaizu, *J. Phys. Chem. A*, 2014, **118**, 3899–3905.
- 17 M. F. Bush, Z. Hall, K. Giles, J. Hoyes, C. V. Robinson and B. T. Ruotolo, *Anal. Chem.*, 2010, **82**, 9557–9565.
- 18 L. Han and B. T. Ruotolo, *Anal. Chem.*, 2015, **87**, 6808–6813.
- 19 B. T. Ruotolo, J. L. P. Benesch, A. M. Sandercock, S. J. Hyung and C. V. Robinson, *Nat. Protoc.*, 2008, **3**, 1139–1152.
- 20 J. K. Jiang, M. D. Chen, C. A. Kuang, M. Attoui and P. H. McMurry, *Aerosol Sci. Technol.*, 2011, **45**, 510–521.
- 21 J. K. Jiang, J. Zhao, M. D. Chen, F. L. Eisele, J. Scheckman, B. J. Williams, C. A. Kuang and P. H. McMurry, *Aerosol Sci. Technol.*, 2011, **45**, II–IV.
- 22 A. Wiedensohler, W. Birmili, A. Nowak, A. Sonntag, K. Weinhold, M. Merkel, B. Wehner, T. Tuch, S. Pfeifer, M. Fiebig, A. M. Fjaraa, E. Asmi, K. Sellegri, R. Depuy, H. Venzac, P. Villani, P. Laj, P. Aalto, J. A. Ogren, E. Swietlicki, P. Williams, P. Roldin, P. Quincey, C. Huglin, R. Fierz-Schmidhauser, M. Gysel, E. Weingartner, F. Riccobono, S. Santos, C. Gruning, K. Faloon, D. Beddows, R. M. Harrison, C. Monahan, S. G. Jennings, C. D. O'Dowd, A. Marinoni, H. G. Horn, L. Keck, J. Jiang, J. Scheckman, P. H. McMurry, Z. Deng, C. S. Zhao, M. Moerman, B. Henzing, G. de Leeuw, G. Loschau and S. Bastian, *Atmos. Meas. Tech.*, 2012, **5**, 657–685.
- 23 F. Carbone, M. Attoui and A. Gomez, *Aerosol Sci. Technol.*, 2016, **50**, 740–757.
- 24 B. Zhao, Z. W. Yang, M. V. Johnston, H. Wang, A. S. Wexler, M. Balthasar and M. Kraft, *Combust. Flame*, 2003, **133**, 173–188.
- 25 H. Lin, C. Gu, J. Camacho, B. Y. Lin, C. Shao, R. X. Li, H. Gu, B. Guan, H. Wang and Z. Huang, *Combust. Flame*, 2016, **172**, 365–373.
- 26 Y. Wang, J. Kangasluoma, M. Attoui, J. Fang, H. Junninen, M. Kulmala, T. Petäjä and P. Biswas, *Proc. Combust. Inst.*, 2017, **36**, 745–752.
- 27 A. Kumar, S. Kang, C. Larriba-Andaluz, H. Ouyang, C. J. Hogan and R. M. Sankaran, *Nanotechnology*, 2014, **25**, 385601.
- 28 J. P. Borra, N. Jidenko, J. Hou and A. Weber, *J. Aerosol Sci.*, 2015, **79**, 109–125.
- 29 S. Jeon, D. R. Oberreit, G. Van Schooneveld and C. J. Hogan, *Analyst*, 2016, **141**, 1363–1375.
- 30 I. W. Lenggoro, B. Xia, K. Okuyama and J. Fernandez de la Mora, *Langmuir*, 2002, **18**, 4584–4591.
- 31 M. Zhu, B. Bendiak, B. H. Clowers and H. H. Hill, *Anal. Bioanal. Chem.*, 2009, **394**, 1853.
- 32 P. R. Kemper, N. F. Dupuis and M. T. Bowers, *Int. J. Mass Spectrom.*, 2009, **287**, 46–57.
- 33 M. Groessl, S. Graf and R. Knochenmuss, *Analyst*, 2015, **140**, 6904–6911.
- 34 S. I. Merenbloom, R. S. Glaskin, Z. B. Henson and D. E. Clemmer, *Anal. Chem.*, 2009, **81**, 1482–1487.
- 35 A. L. Davis, W. Liu, W. F. Siems and B. H. Clowers, *Analyst*, 2017, **142**, 292–301.
- 36 W. Liu, A. L. Davis, W. F. Siems, D. Yin, B. H. Clowers and H. H. Hill, *Anal. Chem.*, 2017, **89**, 2800–2806.

- 37 E. O. Knutson and K. T. Whitby, *J. Aerosol Sci.*, 1975, **6**, 443–451.
- 38 M. R. Stolzenburg and P. H. McMurry, *Aerosol Sci. Technol.*, 2008, **42**, 421–432.
- 39 G. A. Eiceman, E. G. Nazarov, J. E. Rodriguez and J. A. Stone, *Rev. Sci. Instrum.*, 2001, **72**, 3610–3621.
- 40 F. K. Tadjimukhamedov, J. Puton, J. A. Stone and G. A. Eiceman, *Rev. Sci. Instrum.*, 2009, 80.
- 41 H. R. Shamlouei and M. Tabrizchi, *Int. J. Mass Spectrom.*, 2008, **273**, 78–83.
- 42 J. Wang, V. F. McNeill, D. R. Collins and R. C. Flagan, *Aerosol Sci. Technol.*, 2002, **36**, 678–689.
- 43 J. Fernandez de la Mora, L. de Juan, T. Eichler and J. Rosell, *TrAC, Trends Anal. Chem.*, 1998, **17**, 328–339.
- 44 J. Fernandez de la Mora and J. Kozlowski, *J. Aerosol Sci.*, 2013, **57**, 45–53.
- 45 F. Stratmann, T. Kauffeldt, D. Hummes and H. Fissan, *Aerosol Sci. Technol.*, 1997, **26**, 368–383.
- 46 J. K. Jiang, M. Attoui, M. Heim, N. A. Brunelli, P. H. McMurry, G. Kasper, R. C. Flagan, K. Giapis and G. Mouret, *Aerosol Sci. Technol.*, 2011, **45**, 480–492.
- 47 D. R. Collins, D. R. Cocker, R. C. Flagan and J. H. Seinfeld, *Aerosol Sci. Technol.*, 2004, **38**, 833–850.
- 48 P. Dubey and S. Dhaniyala, *Aerosol Sci. Technol.*, 2008, **42**, 544–555.
- 49 P. Dubey and S. Dhaniyala, *Aerosol Sci. Technol.*, 2011, **45**, 1031–1040.
- 50 P. M. Winkler, J. Ortega, T. Karl, P. H. McMurry and J. N. Smith, in *Nucleation and Atmospheric Aerosols*, ed. P. J. DeMott and C. D. Odowd, 2013, vol. 1527, pp. 165–168.
- 51 R. C. Flagan, *Aerosol Sci. Technol.*, 1999, **30**, 556–570.
- 52 M. R. Stolzenburg and P. H. McMurry, *Aerosol Sci. Technol.*, 1991, **14**, 48–65.
- 53 D. R. Oberreit, P. H. McMurry and C. J. Hogan, *Aerosol Sci. Technol.*, 2014, **48**, 108–118.
- 54 D. R. Oberreit, P. H. McMurry and C. J. Hogan, *Phys. Chem. Chem. Phys.*, 2014, **16**, 6968–6979.
- 55 H. Ouyang, S. He, C. Larriba-Andaluz and C. J. Hogan, *J. Phys. Chem. A*, 2015, **119**, 2026–2036.
- 56 K. L. Davidson, D. R. Oberreit, C. J. Hogan Jr. and M. F. Bush, *Int. J. Mass Spectrom.*, DOI: 10.1016/j.ijms.2016.09.013.
- 57 D. R. Chen, D. Y. H. Pui and S. L. Kaufman, *J. Aerosol Sci.*, 1995, **26**, 963–977.
- 58 M. Scalf, M. S. Westphall and L. M. Smith, *Anal. Chem.*, 2000, **72**, 52–60.
- 59 R. Gopalakrishnan, P. H. McMurry and C. J. Hogan, *Aerosol Sci. Technol.*, 2015, **49**, 1181–1194.
- 60 R. Gopalakrishnan, M. J. Meredith, C. Larriba-Andaluz and C. J. Hogan, *J. Aerosol Sci.*, 2013, **63**, 126–145.
- 61 M. Attoui, M. Paragano, J. Cuevas and J. Fernandez de la Mora, *Aerosol Sci. Technol.*, 2013, **47**, 499–511.
- 62 J. M. Thomas, S. He, C. Larriba-Andaluz, J. W. DePalma, M. Johnston and C. J. Hogan, *Phys. Chem. Chem. Phys.*, 2016, **18**, 22962–22972.
- 63 H. Tammet, *J. Aerosol Sci.*, 1995, **26**, 459–475.
- 64 C. Larriba, C. J. Hogan, M. Attoui, R. Borrajo, J. F. Garcia and J. F. de la Mora, *Aerosol Sci. Technol.*, 2011, **45**, 453–467.
- 65 D. R. Chen, D. Y. H. Pui, D. Hummes, H. Fissan, F. R. Quant and G. J. Sem, *J. Aerosol Sci.*, 1998, **29**, 497–509.
- 66 S. Ude and J. F. de la Mora, *J. Aerosol Sci.*, 2005, **36**, 1224–1237.
- 67 S. V. Hering, M. R. Stolzenburg, F. R. Quant, D. R. Oberreit and P. B. Keady, *Aerosol Sci. Technol.*, 2005, **39**, 659–672.
- 68 E. Knutson and K. Whitby, *J. Aerosol Sci.*, 1975, **6**, 443–451.
- 69 G. R. Markowski, *Aerosol Sci. Technol.*, 1987, **7**, 127–141.
- 70 W. Birmili, F. Stratmann, A. Wiedensohler, D. Covert, L. M. Russell and O. Berg, *Aerosol Sci. Technol.*, 1997, **27**, 215–223.
- 71 W. Li, L. Li and D.-R. Chen, *Aerosol Sci. Technol.*, 2006, **40**, 1052–1057.
- 72 P. G. Gormley and M. Kennedy, *Proc. Ir. R. Acad.*, 1949, **52A**, 163–169.
- 73 S. J. Valentine, S. T. Stokes, R. T. Kurulugama, F. M. Nachtigall and D. E. Clemmer, *J. Am. Soc. Mass Spectrom.*, 2009, **20**, 738–750.
- 74 G. Vidal-de-Miguel, M. Macía and J. Cuevas, *Anal. Chem.*, 2012, **84**, 7831–7837.
- 75 G. Steiner and G. P. Reischl, *J. Aerosol Sci.*, 2012, **54**, 21–31.
- 76 G. Biskos, K. Reavell and N. Collings, *Aerosol Sci. Technol.*, 2005, **39**, 527–541.
- 77 P. Kulkarni and J. Wang, *J. Aerosol Sci.*, 2006, **37**, 1303–1325.